Model Predictive Control with Modulated Optimal Vector for a Three-Phase Inverter with an *LC* Filter

Hoach The Nguyen, Eun-Kyung Kim, Ik-Pyo Kim, Han Ho Choi, *Member, IEEE*, and Jin-Woo Jung, *Member, IEEE*

***Abstract*—This paper proposes an effective model predictive control (MPC) scheme using a modulated optimal vector (MOV) and finite control options for a three-phase inverter with an *LC* filter. Unlike other MPC methods, the proposed MPC strategy exploits the unconstrained optimal vector (OV) of the continuous-control-set (CCS) MPC to limit the control options for the unconstrained mode. First, the analytical OV is derived based on a least-squares optimization. If the input constraints are not violated, the OV is applied with a space vector modulation (SVM) technique like the CCS-MPC. Otherwise, the OV is scaled into the MOV and only three control options are online evaluated to reselect the control input. Experiments are conducted on a three-phase inverter test bed with a TI TMS320F28335 digital signal processor to validate the improvements of the proposed method, especially the robust performances and fast responses. The comparative results with the FCS-MPC show the superior performances of the proposed scheme with smaller steady-state error and lower total harmonic distortion due to the analytical OV with SVM, more robustness to parameter uncertainties due to the disturbance observer, and faster dynamic response due to the online reselection of control inputs.**

***Index Terms*—Finite control set (FCS), model predictive control (MPC), modulated optimal vector (MOV), space vector modulation (SVM), three-phase inverter.**

I. Introduction

THREE-PHASE pulse-width modulation (PWM) inverters with *LC* filters are installed in various applications that require high-quality voltage such as distributed generation systems, energy storage systems, and uninterruptible power supplies [1]–[4]. These PWM inverters need advanced control schemes that can guarantee high-quality output voltage in terms of the fast transient response, small steady-state error (SSE), and low total harmonic distortion (THD) under various load conditions, especially step change load, unbalanced load or nonlinear load [5]. Further requirement is the robustness to parameter variations, uncertainties, and noises. A variety of research works have been conducted and reported [6]–[20] on the three-phase inverters with *LC* filters to meet the requirements stated previously.

In the literature, research work on advanced control strategies for three-phase inverters with *LC* filters such as classic feedback control methods [6]–[8], learning-based methods [9]–[12], robust control methods such as sliding mode control and adaptive control [13]–[15], and predictive control methods [16]–[20] have been published. First, the classic feedback control methods use a cascade control structure with a current (inner) control loop and a voltage (outer) control loop [6]–[8]. The outer loop is used to remove the steady-state voltage tracking error normally with proportional-integral (PI) rules [6], whereas the inner loop is used to enhance the closed-loop performance with various control strategies in [7], [8]. These methods are simple in design and inexpensive, but their control performances heavily depend on the gain selection and they cannot either ensure the closed-loop stability or optimize the performances when considering the input constraints. The learning-based methods such as repetitive control [9], [12], interactive learning control [10], and neural network control [11], can improve the steady-state behavior of the controller. However, these control methods are normally slow in dynamic response and time-consuming in learning algorithms. Therefore, a hybrid structure with a high dynamic control method is usually selected for implementation as in [10], [11]. The sliding mode control (SMC) [13] and adaptive control [14], [15] are robust to parameter variations and load disturbances. However, the SMC schemes face difficulties to find out sliding surfaces and other drawbacks are the limited sampling rate and chattering phenomena with variable reference tracking. The adaptive control schemes are also robust to system parameter mismatches but have the computational complexity. The predictive control methods such as deadbeat control [16], [17] and model predictive control have many applications on the three-phase inverters with *LC* filters [18]–[20], especially digital controllers with deadbeat performance. The deadbeat control [17] is widely applied in the voltage control of the three-phase inverters due to its fast dynamic response, simplicity, and straightforward approach. Meanwhile, the model predictive control (MPC) [19], [21]–[25] is flexible with different objectives and constraints. In the view of the MPC, the deadbeat control is a special case of the MPC [18], [19].

The MPC is a promising methodology for researches and applications hence it has gained the sustained development for

Manuscript received December 5, 2016; revised February 21, 2017; accepted April 3, 2017. Date of publication April 13, 2017; date of current version December 1, 2017. This work was supported by the National Research Foundation of Korea under Grant 2015R1A2A2A01003513 funded by the Korea Government (MSIP, Ministry of Science, ICT, and Future Planning). Recommended for publication by Associate Editor T. Geyer. *(Corresponding author: Jin-Woo Jung.)*

H. T. Nguyen, E.-K. Kim, H. H. Choi, and J.-W. Jung are with the Division of Electronics and Electrical Engineering, Dongguk University, Seoul 04620, Korea (e-mail: jinwjung@dongguk.edu).

I.-P. Kim is with the Department of New and Renewable Energy Engineering, Dongguk University, Seoul 04620, Korea.

Color versions of one or more of the figures in this paper are available online at http://ieeexplore.ieee.org.

Digital Object Identifier 10.1109/TPEL.2017.2694049

the last three decades, especially in process control area [26]. In the literature of the MPC for power electronics, there are two main approaches: finite control set (FCS) and continuous control set (CCS). However, there is a knowledge gap between the FCS-MPC and the CCS-MPC. First, the FCS-MPC is simple and straightforward to deal with complicated nonlinear models [19] by simply evaluating all the switching states online. Due to the limited switching states of switch-mode PWM converters, an exhaustive search is affordable in a limited computation time and consequently, the modulation stage is not necessary. However, there are still some drawbacks of the FCS-MPC such as nonzero SSEs [19], [27], [28] (a bounded terminal region), variable power losses, and unwanted resonances due to variable switching frequency [19], [27]. In the other approach called the CCS-MPC, bounded continuous inputs are considered with a modulator in which the MPC optimization is analytically solved offline [29]. The CCS-MPC exhibits good performances in the steady state because the asymptotic stability can be achieved with an explicit solution and a modulation stage [30]. Also, the offline solution of the CCS-MPC can be achieved analytically in case of a linearized model with simple constraints, but not in case of a nonlinear model with more constraints.

To combine the advantages of both approaches, a switched MPC strategy is proposed in [30], which comes from the fact that the FCS-MPC mode with a nonlinear model can direct the system states toward a bounded region of the desired equilibrium state. After that, the control law is switched into the linear CCS-MPC mode with a modulation stage to asymptotically reach the reference values [5], [20]. However, two modes use two separated control laws, so the computed solution from one mode is not utilized in the other mode. In [31], the sphere decoding algorithm (SDA) is improved with reduced execution time by projecting the unconstrained solution onto the envelope of the original FCS to implement the long-horizon FCS-MPC. However, the transformation of spaces in the SDA [31] is still based on a predefined objective function with respect to the unconstrained solution. Therefore, this algorithm cannot achieve the flexibility for the objective function in the transient state. Furthermore, it is a critical problem of the MPC to achieve the robustness against the model mismatches and noises [22]–[24]. A solution based on a hysteresis band is proposed to avoid false triggering due to the noises [30] that make the online computation more complicated. Recent MPC algorithms can achieve some specific features such as more constraints and nonlinear models inclusion [29], [30], online computation reduction [31], [32], fixed switching frequency [33], etc. However, it is still an open issue to find a computationally efficient and robust MPC algorithm [2].

To overcome the issues mentioned above, this paper proposes an efficient MPC method with the modulated optimal vector (MOV) for a three-phase inverter with an *LC* filter. First, the analytical unconstrained optimal vector (OV) is derived using least-squares optimization and then directly used in the unconstrained mode with a space vector PWM (SVPWM) technique like the CCS-MPC. In the constrained mode, the unconstrained solution is scaled into the MOV to inherit both the optimality and offline computation of the unconstrained mode. The benefits of the proposed method are significant in terms of: a simple algorithm with less computational burden, an easy-tuning procedure

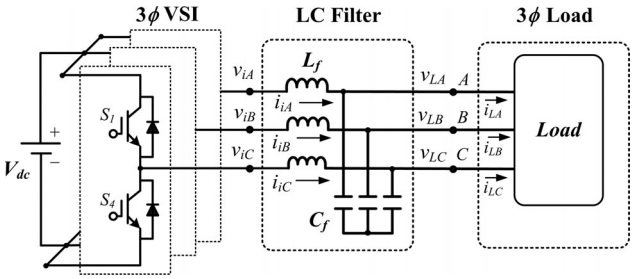

Fig. 1. Three-phase inverter with an *LC* filter.

with two independent modes, flexible objective functions for the modes, a fixed switching frequency, good performances in both steady state and transient state, and robustness to parameter uncertainties. In particular, a simple reselection algorithm for the constrained mode using three candidates (i.e., MOV and two basic vectors with a sector-based switching pattern in SVPWM) is a key strategy, which takes the advantages of CCS-MPC and SVPWM in a fashion like FCS-MPC. In order to validate the performances of the proposed method, the comparative studies between the proposed MPC scheme, the deadbeat control law and the conventional FCS-MPC scheme are conducted in experiments on a prototype three-phase inverter test bed with a TI TMS320F28335 digital signal processor (DSP). Especially, while considering the high uncertainties of the values of both L_f and C_f, the proposed scheme shows the superior voltage regulation performances in terms of smaller SSE, more robustness to parameter uncertainties, lower THD, and faster dynamic response under a fixed switching frequency.

II. Model of Three-Phase Inverter with *LC* Filter

Fig. 1 shows a three-phase inverter with an output *LC* filter where the line-to-neutral inverter voltages and phase currents are denoted by the vectors $\boldsymbol{V}_i = [v_{iA}\, v_{iB}\, v_{iC}]^T$ and $\boldsymbol{I}_i = [i_{iA}\, i_{iB}\, i_{iC}]^T$, respectively. In a similar way, the line-to-neutral load voltage and phase current vectors are represented by $\boldsymbol{V}_L = [v_{LA}\, v_{LB}\, v_{LC}]^T$ and $\mathbf{I}_L = [i_{LA}\, i_{LB}\, i_{LC}]^T$, respectively.

Applying *Kirchhoff's laws* to the *LC* filter, the circuit model of the three-phase inverter is expressed by the following equations in the synchronously rotating $d-q$ reference frame [5], [14]:

$$\begin{cases} \dot{V}_{Ld} = \omega V_{Lq} + k_C I_{id} - k_C I_{Ld}, \\ \qquad\qquad \dot{I}_{id} = -k_L V_{Ld} + \omega I_{iq} + k_L V_{id} \\ \dot{V}_{Lq} = -\omega V_{Ld} + k_C I_{iq} - k_C I_{Lq} \\ \qquad\qquad \dot{I}_{iq} = -k_L V_{Lq} - \omega I_{id} + k_L V_{iq} \end{cases} \tag{1}$$

where $k_C = 1/C_f$ and $k_L = 1/L_f$. In the circuit model (1), V_{id}, V_{iq} are two control inputs, V_{Ld}, V_{Lq}, I_{id}, I_{iq} are four state variables in which V_{Ld}, V_{Lq} are capacitor voltage considered as the controlled outputs, and I_{Ld}, I_{Lq} are load current components considered as the unknown variables.

In the steady state of voltage control applications, the system is expected to work at the equilibrium states determined by

the constant voltage references (i.e., $V_{Ld}^* = \text{constant}$, $V_{Lq}^* = \text{constant}$). The derivative terms of (1) are set to zeros, so the reference inverter currents are inferred as follows:

$$I_{id}^* = I_{Ld} - \omega C_f V_{Lq}^*,\ I_{iq}^* = I_{Lq} + \omega C_f V_{Ld}^*. \tag{2}$$

It is also easy to find out the control inputs (V_{id}, V_{iq}) in the equilibrium states from (1) with given load currents.

The dynamic model (1) is converted into the error dynamic model with new state error variables (i.e., $V_{Lde}, V_{Lqe}, I_{ide}, I_{iqe}$) defined by

$$\begin{cases} V_{Lde} = V_{Ld} - V_{Ld}^* \\ V_{Lqe} = V_{Lq} - V_{Lq}^* \end{cases}, \begin{cases} I_{ide} = I_{id} - I_{id}^* \\ I_{iqe} = I_{iq} - I_{iq}^*. \end{cases} \tag{3}$$

The load current components are assumed to change slowly during a small sampling period ($dI_{Ld}/dt = 0$, $dI_{Lq}/dt = 0$) [5], [15], [19]. Substituting (2) and (3) into (1), then the error dynamic model of the output *LC* filter is derived as

$$\begin{cases} \dot{X}_e = AX_e + BU + BV_i = AX_e + BU + BM_T s \\ Y_e = CX_e \end{cases} \tag{4}$$

where

$$A = \begin{bmatrix} 0 & \omega & k_C & 0 \\ -\omega & 0 & 0 & k_C \\ -k_L & 0 & 0 & \omega \\ 0 & -k_L & -\omega & 0 \end{bmatrix},\ B = \begin{bmatrix} 0 & 0 \\ 0 & 0 \\ k_L & 0 \\ 0 & k_L \end{bmatrix},\ C = \begin{bmatrix} 1 & 0 \\ 0 & 1 \\ 0 & 0 \\ 0 & 0 \end{bmatrix}^T$$

$$M_T = \frac{2}{3} V_{\text{dc}} \begin{bmatrix} \cos\theta & \cos\left(\theta - \frac{2\pi}{3}\right) & \cos\left(\theta + \frac{2\pi}{3}\right) \\ -\sin\theta & -\sin\left(\theta - \frac{2\pi}{3}\right) & -\sin\left(\theta + \frac{2\pi}{3}\right) \end{bmatrix}.$$

X_e $[V_{Lde}, V_{Lqe}, I_{ide}, I_{iqe}]^T$, the state error vector.
V_i $[V_{id}, V_{iq}]^T$, the control input vector representing the continuous manipulated variables for a CCS-MPC approach.
U $[U_d, U_q]^T$, the disturbance vector.
Y_e $[V_{Lde}, V_{Lqe}]^T$, the output error vector.
M_T the transformation matrix of the inverter [19].
θ the transformation angle.
V_{dc} the dc-link voltage.
s the switching states, $s \in [0,0,0]^T, \ldots, [1,1,1]^T$ representing the discrete nature of the switches for an FCS-MPC approach.

Note that the elements of the matrices *(A, B, C)* in (4) are obtained with nominal parameter values of the system. The disturbance vector U is expressed with the nominal values of L_f and C_f below

$$\begin{cases} U_d = \omega L_f I_{Lq} + \left(L_f C_f \omega^2 - 1\right) V_{Ld}^* + d_1 \\ U_q = -\omega L_f I_{Ld} + \left(L_f C_f \omega^2 - 1\right) V_{Lq}^* + d_2 \end{cases} \tag{5}$$

where d_1 and d_2 represent the lumped disturbance due to the parameter uncertainties (including the unmodeled part such as the parasitic resistance in series with the capacitor) and noise. If U_d and U_q are successfully observed as the lumped disturbance vector, the disturbance-rejection approach is implemented for the MPC by compensating for both the predictive model and the control input (V_i) to achieve the robustness. This approach allows the control system design based on uncertain parameters. Therefore, the assumptions in the steady state with constant state variables (2) are held whenever the lumped disturbances are effectively rejected in the control design.

The continuous-time model (4) is converted into the discrete-time model (6)

$$\begin{cases} X_e(k+1) = \Phi X_e(k) + \Gamma U(k) + \Gamma V_i(k) \\ Y_e(k) = CX_e(k) \end{cases} \tag{6}$$

where $\Phi = e^{At_s}$, $\Gamma = \int_0^{t_s} e^{At_s} B dt$, and t_s is the sampling period.

Then, the discrete-time model (6) will be used as the predictive model of the proposed MPC algorithm in Section IV.

III. Discrete-Time Disturbance Observer (DOB) in Form of a Prediction-Type Kalman Filter (KF)

Before giving more details on the load current observer and the DOB, the following three assumptions are needed. First, V_{Ld}, V_{Lq}, I_{id}, and I_{iq} are available. Second, I_{Ld} and I_{Lq} change slowly during a small sampling period [5], [14], [19] in comparison with the system dynamics. Third, the disturbance vector U in (5), which consists of a reference voltage term ($V_{Ld}^* = \text{constant}$, $V_{Lq}^* = \text{constant}$) and a load current term (I_{Ld}, I_{Lq}), also changes slowly during a small sampling period [15]. Therefore, the time derivatives of the load currents (I_{Ld}, I_{Lq}) and the disturbance vector (U) can be set to zero. Note that the state variables V_{Ld}, V_{Lq}, I_{id}, and I_{iq} are not subjected to the assumption that they slowly change during a small sampling period.

A. Load Current Observer

The load currents (I_{Ld}, I_{Lq}) are the main components of the disturbance vector as seen in (5). It should be known to obtain the reference inverter currents and the equilibrium point of the system in (2). Using the current transducers (CTs) in the output load is possible but it makes the overall system more expensive and especially less reliable. With the second assumption mentioned previously, the load current observer has been successfully developed and presented in details in the literature [5], [14], [19]. This paper utilizes the load current observer as the conventional one in [14], [19].

The load current observer is represented by the following equations:

$$\dot{\hat{X}}_0 = A_0 \hat{X}_0 + B_0 U_0 - M\left(Y - C_0 \hat{X}_0\right) \tag{7}$$

where

$$A_0 = \begin{bmatrix} 0 & 0 & 0 & 0 \\ 0 & 0 & 0 & 0 \\ -k_C & 0 & 0 & \omega \\ 0 & -k_C & -\omega & 0 \end{bmatrix},\ B_0 = C_0^T = \begin{bmatrix} 0 & 0 \\ 0 & 0 \\ 1 & 0 \\ 0 & 1 \end{bmatrix},$$

$$\hat{X}_0 = \begin{bmatrix} \hat{I}_{Ld} \\ \hat{I}_{Lq} \\ \hat{V}_{Ld} \\ \hat{V}_{Lq} \end{bmatrix}, U_0 = [k_C I_{id},\ k_C I_{iq}]^T, Y = [V_{Ld},\ V_{Lq}]^T,$$

and $M \in R^{4x2}$ is the observer gain matrix. $\hat{I}_{Ld}$ and $\hat{I}_{Lq}$ are the estimated $d-q$ components of the load currents, respectively.

The details on the load current observer and the optimal gain matrix *M* have been already presented in the literature [5], [14], [19], [20]. It should be noted on the tradeoff between the noise rejection and the bandwidth while choosing the gain matrix. When the statistical properties of the noises are available as the design parameters, a steady-state KF is designed with the optimal gain matrix in [19], [20].

B. Discrete-Time DOB

In this section, the DOB is developed with a predictor–corrector approach. By using the current dynamic equations (i.e., the latter two dynamic equations) of the continuous-time error dynamic model (4) and the third assumption (i.e., the disturbances change slowly) mentioned above, the dynamic model for the DOB is obtained as

$$\dot{X}_d = A_d X_d + B_d U_{d0},\ Y_d = C_d X_d. \tag{8}$$

The continuous-time model (8) is converted to the following discrete-time model (9):

$$X_d(k+1) = \Phi_d X_d(k) + \Gamma_d U_{d0}(k) \tag{9}$$

where

$$\Phi_d = e^{A_d t_s},\ \Gamma_d = \int_0^{t_s} e^{A_d t_s} B_d dt,\ X_d = [U_d,\ U_q,\ I_{ide},\ I_{iqe}]^T$$

$$Y_d = [I_{ide},\ I_{iqe}]^T,\ U_{d0} = [V_{id} - V_{Lde},\ V_{iq} - V_{Lqe}]^T$$

$$A_d = \begin{bmatrix} 0 & 0 & 0 & 0 \\ 0 & 0 & 0 & 0 \\ k_L & 0 & 0 & \omega \\ 0 & k_L & -\omega & 0 \end{bmatrix},\ B_d = \begin{bmatrix} 0 & 0 \\ 0 & 0 \\ k_L & 0 \\ 0 & k_L \end{bmatrix},\ C_d = \begin{bmatrix} 0 & 0 \\ 0 & 0 \\ 1 & 0 \\ 0 & 1 \end{bmatrix}^T.$$

The discrete-time DOB is represented by the following equations:

$$\begin{cases} \hat{X}_d(k+1) = \Phi_d \hat{X}_d(k) + \Gamma_d U_{d0}(k) + L\left[Y_d(k) - C_d \hat{X}_d\right] \\ \hat{U} = \left[\hat{U}_d,\ \hat{U}_q\right]^T \end{cases} \tag{10}$$

where $\hat{X}_d = [\hat{U}_{\rm d},\ \hat{U}_q,\ \hat{I}_{ide},\ \hat{I}_{iqe}]^T$ is the estimated vector, $L \in R^{4x2}$ is the observer gain matrix, and $\hat{U}$ is the estimate of the disturbance vector with its relevant $d-q$ components. As shown in (5), the disturbance vector *U* can be calculated by the formula with the load current term and the reference voltage term. However, in this paper, the disturbance vector is directly estimated and predicted by the discrete-time KF as a lump quantity from the input and output of the system in order to deal with the parameter variations, uncertainties, and noises. It is noted from (10) that both the estimates and one-step-ahead predicted values of the disturbance are simultaneously extracted from the discrete-time observer that is designed with a predictor-corrector technique [34].

The error dynamics of the DOB is obtained from (9) and (10) as follows:

$$X_{\rm de}(k+1) = (\Phi_d - LC_d)\, X_{\rm de}(k) = \Phi_e X_{\rm de}(k) \tag{11}$$

where $X_{de} = X_d - \hat{X}_d$ and $\Phi_e = \Phi_d - LC_d$.

The gain matrix *L* is calculated in the form of a prediction-type KF [34] to minimize the variance of the estimation error in the presence of process and measurement zero-mean white noise with given statistic properties identified by *Q* and *R*

$$L = \Phi_d K C_d^T \left(R + C_d K C_d^T\right)^{-1} \tag{12}$$

where *K* is the covariance matrix of the estimation error, which is also the solution of the following discrete-time algebraic Riccati equation (DARE):

$$\Phi_d K \Phi_d^T - \Phi_d K C_d^T \left(R + C_d K C_d^T\right)^{-1} C_d K \Phi_d^T - K + Q = 0. \tag{13}$$

Considering (12), the DARE (13) can be rewritten as follows [34]:

$$\begin{aligned} &(\Phi_d - LC_d)\, K (\Phi_d - LC_d)^T + \mathrm{LRL}^T - K + Q = 0 \\ &\quad \Leftrightarrow\ \Phi_e K \Phi_e^T - K = -\mathrm{LRL}^T - Q. \end{aligned} \tag{14}$$

The DARE (14) indicates that there exists a positive-definite matrix *K* with given *R* and *Q*, such that

$$\Phi_e K \Phi_e^T - K < 0. \tag{15}$$

Let the Lyapunov function be selected as the following:

$$\begin{aligned} V_d(k) &= X_{\rm de}^T K X_{\rm de} \\ \Delta V_d &= V_d(k+1) - V_d(k) = X_{\rm de}^T (\Phi_e^T K \Phi_e - K) X_{\rm de} \le 0. \end{aligned} \tag{16}$$

As indicated in (16), ΔV_d is negative or equal to zero only at $X_{\rm de} = 0$. This implies that the matrix Φ_e is stable. In other words, the DOB guarantees the global asymptotic stability that ensures the estimation errors to converge to zero.

Remark 1: Gaussian white-noises from the system and measurements (ξ, η) are taken into account in the KF [5], [14], [20], and then (6) can be rewritten as follows:

$$\begin{cases} X_d(k+1) = \Phi_d X_d(k) + \Gamma_d U_{d0}(k) + \xi \\ Y_d(k) = C_d X_d(k) + \eta \end{cases}. \tag{17}$$

The observer gain matrix *L* is selected to minimize the steady-state covariance by solving the DARE (13), which is tuned by adjusting the design matrices $Q = \mathrm{E}(\xi\xi^T)$ and $R = \mathrm{E}(\eta\eta^T)$ in (12) and (13), respectively. That is, *Q* is tuned by gradually increasing its values to achieve the desired fast convergence, whereas *R* is tuned by decreasing its values with expected less-noise measurements until the observer performance is achieved satisfactorily. In case of large *Q* (i.e., significant model noise) and small *R* (i.e., small measurement noise), *L* is large, so a fast observer with a high bandwidth can be achieved. Due to the separation principle [34], the DOB gain matrix can be selected independently from the controller gain matrix with the desired additional poles in the closed-loop system. Consequently, the importance of the DOB is manifold as follows: simplify the model for the controller design, improve the overall control performances with the disturbance rejection approach (especially the robustness), and improve the stability [34], [35].

IV. Model Predictive Voltage Controller Design with MOV

A. Observer-Based Prediction

It is assumed that the proposed predictive control algorithm causes one sampling-time delay. Therefore, one-step-ahead prediction is set to compensate for this delay. First, the load currents are estimated as $\hat{I}_{Ld}(k)$, $\hat{I}_{Lq}(k)$ by the observer. Then the reference inverter currents are calculated from (2) as $I^*_{id}(k)$, $I^*_{iq}(k)$, and the state error $X_e(k)$ at time step k is calculated from (3). At the same time, the estimated and predicted disturbance values $\hat{U}(k)$, $\hat{U}(k+1)$ are directly obtained from the observer (10). The one-step-ahead prediction $X_e(k+1)$ of the state error is calculated by using (6). Once more, the two-step-ahead prediction $X_e(k+2)$ of the state error is represented by

$$X_e(k+2) = C_X(k) + \Gamma V_i(k+1) \tag{18}$$

where

$$C_X(k) = \Phi^2 X_e(k) + \Phi\Gamma\hat{U}(k) + \Phi\Gamma V_i^*(\mathrm{k}) + \Gamma\hat{U}(k+1) \tag{19}$$

and $V_i^*(k)$ is the control input applied during the kth sampling period, which is calculated by the predictive controller at the previous time step $(k-1)$. $C_X(k)$ and Γ in (18) are four-column matrices that can be decomposed as

$$C_X(k) = \left[C_{12}^T(k),\ C_{34}^T(k)\right]^T \in R^{4\times 1},\ \Gamma = \left[\Gamma^T{}_{12},\ \Gamma^T{}_{34}\right]^T \in R^{4\times 2}$$

The predicted voltage vector is extracted from (17) as

$$V_{Le}(k+2) = C_{12}(\mathrm{k}) + \Gamma_{12} V_i(k+1) \tag{20}$$

where $V_{Le}(k+2) = [V_{Lde}(k+2), V_{Lqe}(k+2)]^T$.

B. MPC Optimization Problem and Unconstrained Solution

The optimization problem of the MPC can be summarized with the proposed objective function as follows:

$$V_i^*(k+1) = \arg\min \left(\|V_{Le}(k+2)\|^2 + \mu \left\| V_i(k+1) + \hat{U}(k+1) \right\|^2 \right) \tag{21}$$

subject to (20) and (22).

where $\mu \in [0, 1] \subset R$ is the only weighting factor, $\hat{U}(k+1) = [\hat{U}_d(k+1), \hat{U}_q(k+1)]^T$ is the disturbance vector, and $\|.\|$ is the Euclidean norm.

In case of using an SVPWM technique, the input voltage vector has the following theoretical constraints [20]:

$$\sqrt{3}\,|V_{i\alpha}(k+1)| + |V_{i\beta}(k+1)| \le \frac{2}{\sqrt{3}} V_{\mathrm{dc}},\ |V_{i\beta}(k+1)| \le \frac{V_{\mathrm{dc}}}{\sqrt{3}} \tag{22}$$

where $V_{i\alpha}, V_{i\beta}$ are the components of the voltage input vector in the stationary $\alpha-\beta$ reference frame and V_{dc} is the dc-link voltage. Note that this paper focuses on the control input constraints as strict constraints like [19], [20], whereas other constraints can be handled by the proposed online reselection process in the constrained mode. However, the other constraints are not critical, which are subjected to the protection functions of other software and hardware such as relays and circuit breakers.

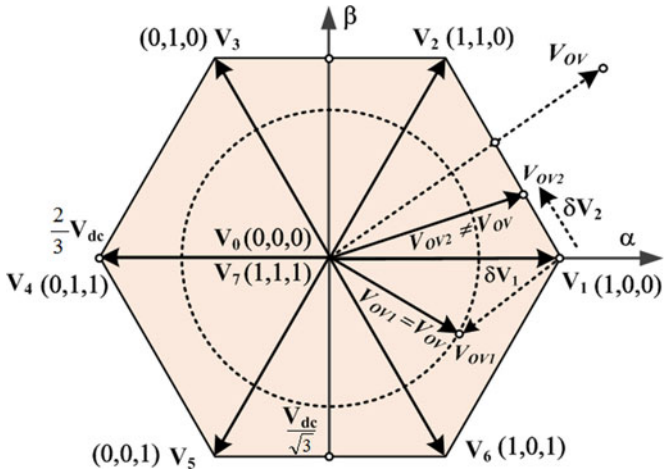

Fig. 2. Error vectors between the conventional FCS solution and the CCS explicit solution in two different operating modes considering the control input constraints in a three-phase inverter.

The constraint (22) represents a feasible set for the input control vector $V_i(k+1)$ as a convex set in a hexagon as shown in Fig. 2. The objective function in (21) is obviously convex as a positive quadratic function.

By directly substituting (20) into (21), the objective function in (21) can be rewritten as follows:

$$J = \|C_\mu + \Gamma_\mu V_i(k+1)\|^2 \tag{23}$$

where $C_\mu = \begin{bmatrix} C_{12}(k) \\ \mu\hat{U}(k+1) \end{bmatrix} \in R^{4\times 1}$, $\Gamma_\mu = \begin{bmatrix} \Gamma_{12} \\ \mu I_{2\times 2} \end{bmatrix} \in R^{4\times 2}$, and $I_{2\times 2}$ is the 2×2 identity matrix.

Temporally neglecting the constraint (22), the optimization problem (21) is now considered as a free-constrained least-squares problem with the objective function (23). It is noted that Γ_μ is a tall matrix and has independent columns. Therefore, the Gram matrix $\Gamma_\mu^T\Gamma_\mu$ is invertible. The unique least-squares solution of this unconstrained problem is called the unconstrained OV

$$V_{OV}(k+1) = -\left(\Gamma_\mu{}^T\Gamma_\mu\right)^{-1}\Gamma_\mu{}^T C_\mu. \tag{24}$$

The solution (24) depends on two types of data. First, the offline data (Φ, Γ) depend only on the nominal parameters of the system. Next, the online data including $X_e(k)$, $V_i^*(k)$, $\hat{U}(k)$, and $\hat{U}(k+1)$ depend on the current states of the system. In the OV (24), the matrix $(\Gamma_\mu^T\Gamma_\mu)^{-1}\Gamma_\mu^T$ and most components of C_μ in (23) such as Φ^2, $\Gamma\Phi$, and Γ in (19) can be also prepared offline in advance as the constants in real-time implementation. Meanwhile, the online data is continuously updated with a receding horizon policy of the MPC. Therefore, this remark should be considered appropriately to achieve a computational efficiency and obtain the OV (24) in real-time applications.

Remark 2: When considering a special case with $\mu = 0$, the global minimum of the objective function (23) is zero. In this case, the general optimal solution (23) now becomes the solution of the algebraic (23), $J = 0$ and this solution (24) offers the deadbeat control law [18], [20], [35].

C. MOV with Simplified Finite Control Options

This section elaborates an approach to achieve the optimality in the constrained mode that takes the input constraints (22) into account via an online solution to deal with the online changes of an objective function (21) in the constrained mode. First, the conventional FCS approach is analyzed as a motivation for the proposed approach. Then, a new algorithm is derived by integrating the MOV, the sector-based SVPWM technique, and the online evaluation in a fashion like FCS-MPC to improve the control performance.

Fig. 2 shows the error vectors (in view of an ideal CCS-MPC with a modulator) created by the conventional FCS algorithm in two different operating modes considering the input control constraint (22) in a three-phase inverter. The explicit solution of the MPC optimization problem (21) for each mode is assumed to be found, which is represented by $V_{\mathrm{OV}1}$ and $V_{\mathrm{OV}2}$ as shown in Fig. 2. In the first operating mode illustrated in Fig. 2, the constraint (22) is satisfied when the global optimal solution V_{OV} (24) locates inside the hexagon, so V_{OV} is feasible for the constrained optimization problem (21) (i.e., $V_{\mathrm{OV}1} = V_{\mathrm{OV}}$), which mathematically achieves the global minimum at $V_{\mathrm{OV}1}$. This is the mode when the system works in the steady state (i.e., V_{OV} draws a circular locus as shown by the dashed circle in Fig. 2) or in some transient states near the equilibrium point. Even though the explicit solution $V_{\mathrm{OV}1}$ can be calculated by (24), the conventional FCS algorithm cannot select $V_{\mathrm{OV}1}$, which does not belong to the FCS (i.e., $V_0, V_1, \ldots, V_7$). In Fig. 2, the best candidate vector provided by the conventional FCS algorithm would be V_1 associated with an error (i.e., $\delta V_1 = V_{\mathrm{OV}1} - V_1$). In practical applications, the error δV_1 can be considerable if the difference between the dc-link voltage and the equilibrium control input (V_i^*) is large. Note that this error critically degrades the control quality of the output voltage, especially with the high THDs and large SSEs in the steady state [2], [19]. In the second operating mode, the constraint (22) is violated when the global optimal solution V_{OV} locates outside the hexagon as shown in Fig. 2, so V_{OV} is not feasible for the optimization problem (21) (i.e., $V_{\mathrm{OV}2} \neq V_{\mathrm{OV}}$). This is the mode that the system works in some transient states far from the equilibrium point and a large control input is required to direct the system to the equilibrium. As depicted in Fig. 2, the constrained optimization problem (21) achieves the minimum at the constraint border with $V_{\mathrm{OV}2}$. However, the conventional FCS algorithm cannot exactly select $V_{\mathrm{OV}2}$, which does not always belong to the FCS. In Fig. 2, the best candidate vector provided by the conventional FCS algorithm would be V_1 associated with an error (i.e., $\delta V_2 = V_{\mathrm{OV}2} - V_1$). Note that the conventional FCS algorithm can select the maximum possible control input among the six active vectors (i.e., $V_1, V_2, ..., V_6$) to achieve the fast dynamic response [28]. However, the error δV_2 with amplitude and phase components can degrade the transient response properties due to overshoot and long settling time. In case that the sampling and switching frequencies are low, both δV_1 and δV_2 are applied in a long period of time, which worsens the control output quality. In summary, the errors (δV_1 and δV_2) generated by the conventional FCS algorithm in both modes can deteriorate both the steady-state and transient-state performances.

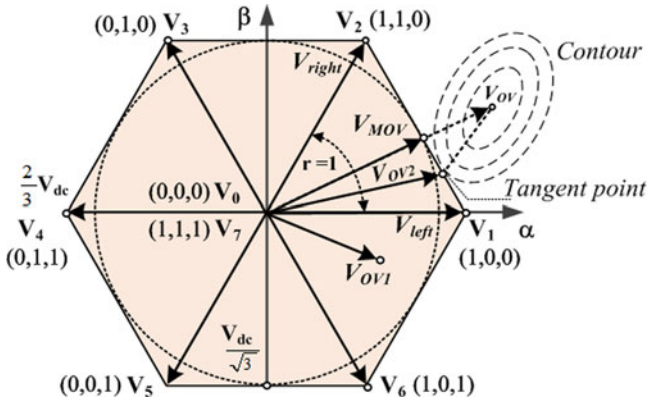

Fig. 3. Modulated optimal voltage vector with the proposed MPC considering the control input constraints in a three-phase inverter.

Fig. 3 shows the modulated optimal voltage vectors with the proposed MPC considering the control input constraints in a three-phase inverter to deal with the error vectors (δV_1 and δV_2) as mentioned in the previous paragraph. Unlike the conventional FCS-MPC, the global optimal solution (V_{OV}) is calculated by (24) and effectively utilized by the proposed MPC algorithm to improve both the steady-state and transient-state performances. In the first operating mode described in Fig. 3, V_{OV} (24) is directly applied with an SVPWM technique if the constraint (22) is satisfied, and then the error vector is eliminated (i.e., $\delta V_1 = V_{\mathrm{OV}1} - V_{\mathrm{OV}} = 0$). Meanwhile, in case that the constraint (22) is violated, V_{OV} is scaled into V_{MOV} and the simplified control set (i.e., V_{left}, V_{MOV}, and V_{right}) is directly evaluated to reselect the OV, $V_{\mathrm{OV}2}$. Note that the V_{left} and V_{right} are two basic vectors of the sector r where V_{OV} locates (i.e., V_1, V_2, and V_{MOV} with $r = 1$ in Fig. 3). As illustrated in Fig. 3, the constrained OV ($V_{\mathrm{OV}2}$) is determined by the tangent point between the hexagonal boundary and the contour of the quadratic objective function. The optimality associated with $V_{\mathrm{OV}2}$, which can be located using the SDA in [31], is only for a predefined objective function of the unconstrained mode. Furthermore, the implementation of $V_{\mathrm{OV}2}$ in the CCS-MPC needs a modulator with an assumption on high enough switching frequency [35]. However, this paper proposes a direct method like FCS-MPC that can track a new objective function in the constrained mode to achieve the transient performance different from the steady-state performance. In this paper, a simple reselection algorithm is proposed to take the advantages of the OV, the discrete switching states, and the sector-based PWM. That is, the hexagonal constraint boundary is simplified into the inner circle of the hexagon (i.e., the dashed circle in Fig. 3) and the number of the candidate vectors is reduced

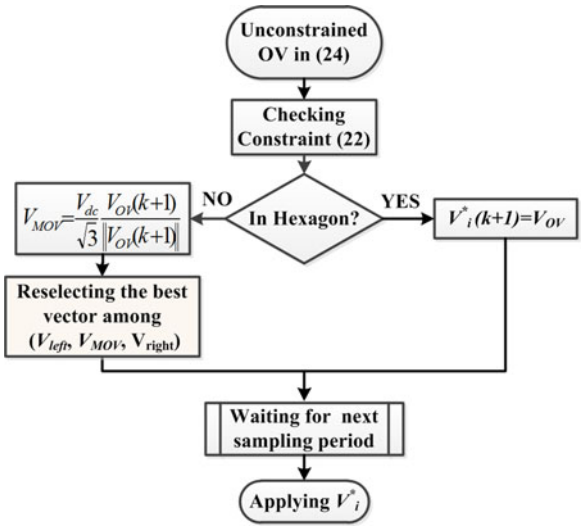

Fig. 4. Flowchart of the proposed MPC algorithm with the MOV.

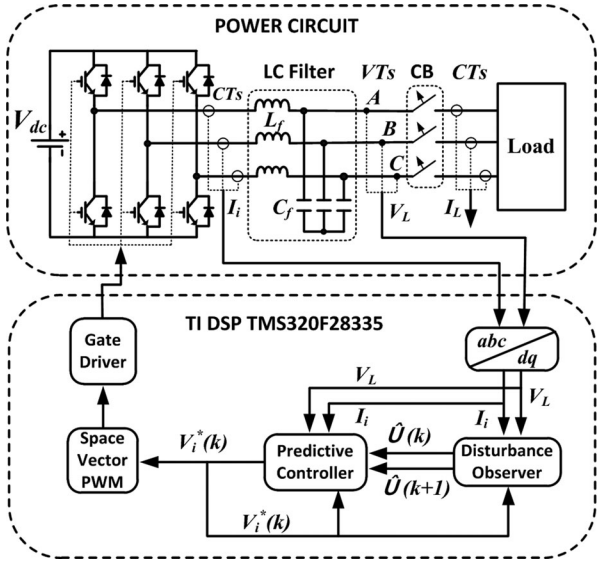

Fig. 5. Experimental setup with a prototype three-phase inverter test bed.

from five to three. Note that the space vector modulation (SVM) cannot reach all the hexagon space due to the limited switching frequency of the power transistors and the unavoidable delay. Therefore, the boundary is often simplified as the inner circle shown in Fig. 3 [20] considering the practical implementation of the SVM.

For example, as shown in Fig. 3, if the $V_{\rm OV}$ (24) belongs to the region 1 ($r = 1$) then the tangent point should locate somewhere on the boundary of the combined region of three sectors (i.e., 6, 1, and 2) only because both the contour and the constraint are convex, so the new FCS should be a five-element set (i.e., V_6, V_1, $V_{\rm MOV}$, V_2, and V_3). In an SVPWM, a maximum reference vector such as $V_{\rm OV2}$ in the sector ($r = 1$) is realized by only two basic vectors (V_1, V_2) within one switching period. Therefore, only these two vectors are selected in addition to the MOV for an online evaluation. Note that the online evaluation is not limited to the predefined objective function of the unconstrained mode [31], and an independent and online configured objective function can be tracked by the constrained mode to achieve the desired transient performance. In this mode, the control algorithm is efficient in computation due to the simplified finite control options with only three candidates (i.e., $V_{\rm left}$, $V_{\rm MOV}$, $V_{\rm right}$), especially the $V_{\rm MOV}$ is already known from the unconstrained mode.

Note that the proposed method is different from the switched MPC [30] because of the following: first, the unified model (6) is utilized for both modes with the disturbance-rejection approach; second, the constrained mode inherits the scaled OV with the SVM (named as the MOV) from the unconstrained mode; third, the direct evaluation algorithm uses the finite control options with only three candidates; finally, the hysteresis band is not needed due to the DOB.

Fig. 4 shows the flowchart of the proposed MPC algorithm with the MOV described in this paragraph. Then, the overall design procedure for the proposed MPC method is summarized as follows:

1) identifying the constant matrices (A, B, C) of the continuous-time error dynamic model (4);
2) converting the continuous model (4) into the discrete model (6) by using MATLAB;
3) selecting the weight matrices Q and R in (12) and (13) and then tuning the observer gain matrix L in (10) as shown in *Remark 1*;
4) preparing the offline data: Φ^2, $\Phi\Gamma$, Γ_μ, $(\Gamma_\mu^T\Gamma_\mu)^{-1}\Gamma_\mu^T$ as mentioned in *Remark 2* to form the online global OV $V_{\rm OV}$ (24) with respect to the specific objective function and weighting factor μ in (21);
5) following the algorithm in Fig. 4 to obtain the OV $V_i^*(k+1)$.

The overall stability of the proposed MPC method is ensured in which the finite-control-option-based selection drives the system to a bounded terminal region [25], [30] where the unconstrained optimal solution (24) no longer violates the input constraints (22). In the bounded terminal region (i.e., the input constraints are released), the unconstrained optimal solution ensures the asymptotic stability [5], [30].

Remark 3: In a special case that the contours in Fig. 3 are circles, the MOV is the explicit solution for the constrained mode because the tangent point of two circles locates on the connecting-centers line, $V_{\rm MOV} = V_{\rm OV2}$. This case represents only a specific case of the objective function as shown in [20], which is also the simplest case for the online computing algorithm. In a general case of the objective function (21), the MOV is inherited from the unconstrained solution (24) to reduce the online computation. In this paper, the proposed method aims at using the direct online evaluation (in a fashion like FCS-MPC) in the constrained mode to deal with the changes of the objective function, the constraints, and the model (even change to a nonlinear model), so an optimal explicit solution is needed only for the unconstrained mode, but not for all the operating range like [29], [30].

V. Comparative Experimental Results

A. Experiment Platform

Fig. 5 shows the experimental setup with a prototype three-phase inverter test bed including the power circuit and the DSP-based control system. First, the power circuit comprises of a 2-kVA class three-phase inverter, a dc-link ($V_{\rm dc} = 295$ V), a *LC* filter ($L_f = 10$ mH, $C_f = 6.6$ μF), and prototype loads. Next, the digital control system with a 16-bit floating-point TI TMS320F28335 DSP receives the measured inverter current and load voltage feedbacks from the CTs and voltage transducers and gives the control signals to the insulated-gate bipolar transistor (IGBTs) of the three-phase inverter via an SVPWM technique and a gate driver. In this paper, the control algorithm is implemented to ensure a fundamental frequency of 60 Hz and a line to neutral voltage of 110 $V_{\rm rms}$ for the load.

B. Observer Gains and Weighting Factor Selection via Closed-Loop Dynamic Responses

This section elaborates the selection of the observer gain *L* and the weighting factor μ by experimentally monitoring the closed-loop dynamic responses upon the reference step-change from 0 $V_{\rm rms}$ to 110 $V_{\rm rms}$ at no-load condition. The dependence of the closed-loop behavior on the observer gain *L* and the objective weighting factor μ is analyzed and then verified by the experimental results.

First, the DOB performance depends on the gain matrix $L \in R^{4\times 2}$, which is optimally calculated from the covariance matrixes indicating the statistics properties $Q = \mathrm{E}(\xi\xi^T)$ and $R = \mathrm{E}(\eta\eta^T)$. The DOB gain is selected via adjusting $Q = \mathrm{E}(\xi\xi^T)$ and $R = \mathrm{E}(\eta\eta^T)$ in (12) and (13), respectively. With low noise measurements, *Q* can be tuned with high values, whereas *R* is tuned with small values to achieve the desired fast convergence. In case of large *Q* and small *R* (i.e., small measurement noise), the observer gain *L* is high, so a fast observer can be achieved. But in return, the noise rejection capability is reduced [19]. Therefore, to take the advantages of the noise filtering of the DOB, a fine tuning technique is needed via experiments. For simplicity, *R* is fixed as the identity matrix, i.e., $R = I_{2\times 2}$ and *Q* is adjustable, i.e., $Q = \lambda I_{4\times 4}$ via the weighting factor λ.

Second, there is a tradeoff between the control performances and the control efforts [5] in optimal control as shown in (21) with the relative factor μ. As mentioned in *Remark 2*, the proposed control method becomes the deadbeat control as the most aggressive controller by simply setting $\mu = 0$. Theoretically, the output voltage can be set to the reference values within two sampling periods (i.e., the order of *LC* filter model is two) as the fastest settling time can be achieved. However, the deadbeat control is very sensitive to model uncertainties, parameter perturbation, and measurement noise [18], [20]. Despite the fact that the DOB can increase the stability margin, the deadbeat control law can result in the instability due to its aggressive reaction against unpredicted noises [20].

Meanwhile, the disturbance vector is estimated with the DOB (10) and directly compensated for by the control input as shown in the second term of the objective function (21). As long as μ increases, the disturbance compensation term increases, then the control performance is less sensitive to noises and uncertainties but in return, the dynamic response of the controller is slow. Unfortunately, the uncertainties, parameter variations, and noises are unknown meanwhile the fast dynamic response is desired. Therefore, the tuning procedure of the weighting factor μ should be implemented experimentally on the test bed by investigating the control performances with a step-change of the reference inputs from 0 $V_{\rm rms}$ to 110 $V_{\rm rms}$ at no-load condition. The weighting factor tuning starts with $\mu = 1$ and then μ is further decreased depending on the noise level of the experimental setup until the desired performances are obtained experimentally. It is worth to note that the gain tuning of the proposed method is much simpler than the conventional PI control [6] and the optimal control linear-quadratic regulator (LQR) [5] due to two independent modes (i.e., constrained mode and unconstrained mode) with different objective functions. The unconstrained mode can be fixed with an offline objective function, whereas the constrained mode can track a flexible online objective function via only one scalar weighting factor in a limited range [0, 1].

Finally, Fig. 6 shows the closed-loop performances of the proposed MPC method with a step-change reference at no-load condition to confirm the assessment mentioned above. Fig. 6(a) illustrates the load phase voltage error ($v_{LA} - v^*_{LA}$) dynamics under different gain scenarios by changing the weighting factor λ. In this figure, when increasing the matrix *Q* (i.e., increasing the observer gain *L*), the load voltage error converges more quickly. However, in return, when *Q* is large (i.e., large λ), there are some noises in the dynamics. Therefore, an appropriate observer gain is obtained with $\lambda = 1\mathrm{e}^9$ for the experimental setup as shown in Fig. 6(a). Next, Fig. 6(b) shows the tracking responses of the load phase voltage ($v_{\rm LA}$) and *d*-axis voltage (V_{Ld}) with different weighting factor μ. When $\mu = 1$, the output waveforms exhibit good steady-state performance with less distortion and small error, but the dynamic response in transient state is quite slow. On the other hand, when $\mu = 0.005$, a fast dynamic response is observed during the transient, but the aggressive behavior of the controller is sensitive to the noises, so the DOB takes longer time to suppress these disturbances to stabilize the system. However, when $\mu = 0$ (i.e., deadbeat control law), even with the help of the DOB, the system exhibits the instability. To compromise these differences, the weighting factor is tuned around the value $\mu = 0.1$. However, the proposed MPC method can achieve the advanced performances with two different settings in two modes (i.e., unconstrained mode and constrained mode). Fig. 6(c) shows the closed-loop dynamic performance with final tuning values (i.e., $\mu = 0.15$ in the unconstrained mode to achieve a good steady-state regulation and $\mu = 0.015$ in the constrained mode to achieve a fast dynamic response). In Fig. 6(c), the good performances are attained by showing the small steady-state errors (0.8%) at both references, fast reference voltage tracking (within about 1.2 ms) with small overshoot, and low THD (0.2%). Note that in this figure, the load $d-q$ axis voltage (V_{Ld}, V_{Lq}) and the Euclidean norm of the control input (V_i) gradually reach a steady-state value and keep stable with a small overshoot. In practice, these tracking performances are deserved well because the control input does

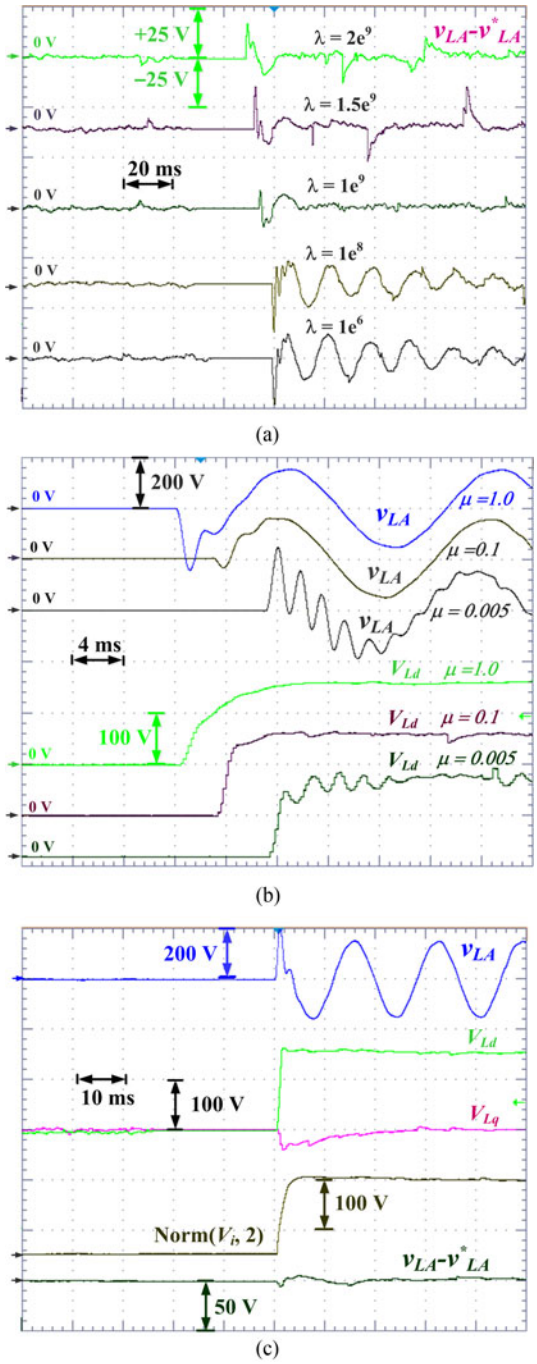

Fig. 6. Closed-loop performances of the proposed MPC method with a step-change reference at no-load condition. (a) Load phase voltage error ($v_{LA} - v^*_{LA}$) dynamics with different weighting factors, λ. (b) Load phase voltage (v_{LA}) and *d*-axis voltage (V_{Ld}) tracking dynamics with different weighting factor μ. (c) Closed-loop dynamic response with final tuning values (i.e., $\lambda = 1e^9$, $\mu = 0.15$ for the unconstrained mode, and $\mu = 0.015$ for the constrained mode).

not generate any voltage pulse that harms the voltage insulation of the power switching devices.

C. Robustness Against Parameter Uncertainties

This subsection evaluates the robustness of the proposed MPC method by investigating the insensitivity of the

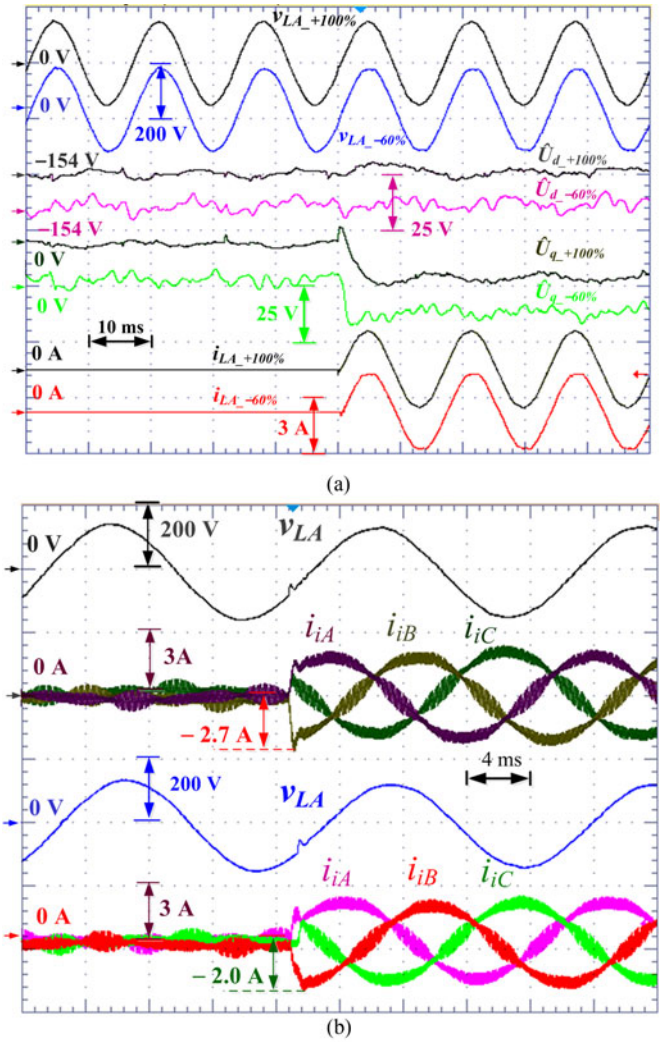

Fig. 7. Robustness and constraints regulating capability of the proposed MPC method. (a) Experimental waveforms of the two different designs (i.e., +100% and –60% uncertainties in both L_f and C_f). (b) Inverter currents in case of uncritical (upper waveforms) and critical (lower waveforms) constraints.

controlled output against parameter uncertainties under load step-change conditions. In this paper, the parameter variations are considered with two control designs that are derived from different *LC* values but implemented on the same experimental setup under the same scenario (i.e., load sudden change from no-load to full-load) [22]. The first design (*Design 1*) is selected with +100% parameter uncertainties (i.e., $L_f = 2.0 \times 10 = 20$ mH, $C_f = 2.0 \times 6.6 = 13.2\,\mu$F). Next, the second design (*Design 2*) is chosen with –60% parameter variations (i.e., $L_f = 0.4 \times 10 = 4$ mH, $C_f = 0.4 \times 6.6 = 2.66\,\mu$F). It is noted that since the most common tolerances of the *LC* values are only within ±10% around the nominal values provided by the manufacturers [5], these two designs are selected in this paper to make more challenge to the controller with severe parameter uncertainties.

In this paper, the output insensitivity is evaluated by three criteria of the output voltage (i.e., RMS values, frequencies, and THDs). Fig. 7(a) shows the experimental waveforms of the two different designs mentioned above. This figure displays the

phase *A* load voltage (v_{LA}), estimated disturbances ($\hat{U}_d$, $\hat{U}_q$), and phase *A* load current (i_{LA}). As shown in Fig. 7(a), the waveforms of *Design 1* (upper positions) and *Design 2* (lower positions) are experimentally captured and then measured by using a digital oscilloscope. In this figure, the RMS values of the phase *A* voltage are measured as 109.8 $V_{\rm rms}$ ($v_{LA_{+100\%}}$) and 109.6 $V_{\rm rms}$ ($v_{LA_{-60\%}}$), respectively. Also, the measured frequencies of *Design 1* and *Design 2* are 60.01 and 60.02 Hz, respectively. Next, the measured THD values of the two output voltages ($v_{LA_{+100\%}}$, $v_{LA_{-60\%}}$) are observed as 1.1% and 1.2%, respectively. It is noted that these slight differences exhibit the insensitivity of the proposed MPC method against parameter uncertainties. To this end, the proposed MPC method can overcome the main drawback of the MPC, i.e., the heavy dependency on parameters accuracy [2]. Fig. 7(b) shows the experimental waveforms of the three-phase inverter currents $\boldsymbol{I}_i = [i_{iA}\, i_{iB}\, i_{iC}]^T$ to prove the capability of the proposed MPC method that can deal with other constraints in two cases. The first case's waveforms are shown in the upper positions where the constraints are uncritical because the inverter current limits are indirectly treated by the algorithm via input constraints. The second case's waveforms are shown in the lower positions where the constraints are critical by narrowing down the voltage limits $|\boldsymbol{V}_C| \leq (155.6 \pm 20\%)\,\text{V}$, the current limits $|\boldsymbol{I}_i| < 2.0\,\text{A}$. Note that these limits are intentionally made below the limits to be set for voltage and current protection devices (i.e., overvoltage protection and overcurrent protection with thermal trip) in order to evaluate the effectiveness of the proposed MPC scheme on dealing with these constraints. In this case, the assumed critical constraints are directly included in the control algorithm by adding the pruning term (high penalty) on these constraints to the objective function in the constrained mode. The experimental waveforms in Fig. 7(b) confirm the fact that all the constraints are treated well with new limits and the transient response gets slower as the constraints are more critical.

The key factor that contributes to this robustness is the effective performance of the KF-based disturbance observer [17], [34]. As shown in Fig. 7, the disturbance terms of *Design 1* (i.e., $\hat{U}_{d_+100\%}$, $\hat{U}_{q_+100\%}$) have less ripple than those of *Design 2* (i.e., $\hat{U}_{d\_60\%}$, $\hat{U}_{q\_60\%}$), but they have the same waveform patterns that successfully catch up with the load-current change. To comprehensively investigate the robustness of the proposed approach, the following Section V-D will present more detailed results with $+50\%$ uncertainty of L_f and -50% uncertainty of C_f.

D. Comparative Case Studies

In order to prove the improvements of the proposed MPC method, this section shows the comparative results between the conventional FCS-MPC scheme and the proposed MPC scheme. In this paper, the proposed MPC technique uses the sampling frequency of 30 kHz and a fixed switching frequency of 5 kHz with the SVPWM technique, whereas the conventional FCS scheme uses the same sampling frequency of 30 kHz but a variable switching frequency to ensure the average switching frequency at about 5 kHz [27]. Note that the fast sampling is the bottle neck for implementing the conventional FCS algorithm because the allowable time for algorithm computation is limited by the sampling period [19]. For a fair comparison, the experiments are conducted with the sampling frequency of 30 kHz for FCS-MPC [19] with TI TMS320F28335 to prove the less complexity of the proposed algorithm. Despite the fact that the proposed MPC method requires less online computation compared with the conventional FCS-MPC so it can works with a higher sampling rate, the sampling rate should be chosen appropriately considering the capability of the digital platform and the control performance. It is well known that the fixed switching scheme is preferable to the variable switching scheme in practical applications because the latter has some disadvantages such as difficult electromagnetic interference (EMI) filter design, uneven switching loss-distribution over the switches, unwanted resonances due to the self-resonance frequency of the *LC* filter [2], etc.

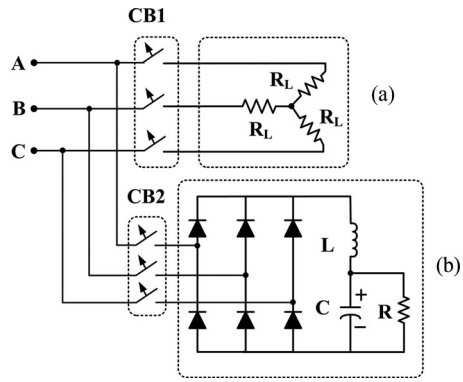

Fig. 8. Loads of an experiment platform. (a) Three-phase resistive load with star-connected resistors. (b) Nonlinear load with a three-phase diode rectifier.

As illustrated in Fig. 8, experiments are performed on two different kinds of loads: a resistive load and a diode rectifier load. Fig. 8(a) shows a three-phase load with a resistor ($R_L = 70\,\Omega$) per phase, whereas Fig. 8(b) depicts a three-phase full-bridge diode–rectifier load with an inductor ($L = 10$ mH), a capacitor ($C = 330\,\mu$F), and a resistor ($R = 200\,\Omega$).

In this paper, the following cases provide comprehensive comparative results under different types of the load conditions:

Case 1: Step-change load under model uncertainties with $+50\%L_f$ and $-50\%C_f$.

Case 2: Unbalanced load under model uncertainties with $+50\%L_f$ and $-50\%C_f$.

Case 3: Nonlinear load under model uncertainties with $+50\%L_f$ and $-50\%C_f$.

Case 1 demonstrates the transient- and steady-state performances in case that the three-phase resistive load is abruptly applied to the inverter. Next, *Case 2* shows the transient- and steady-state performances when phase *A* is suddenly opened. Finally, *Case 3* is also selected to show the steady-state performances in case of a three-phase diode rectifier. To comprehensively verify the robustness under parameter uncertainties in addition to Section V-C, model uncertainties with $+50\%L_f$ and $-50\%C_f$ distortions are set under all investigated cases. That

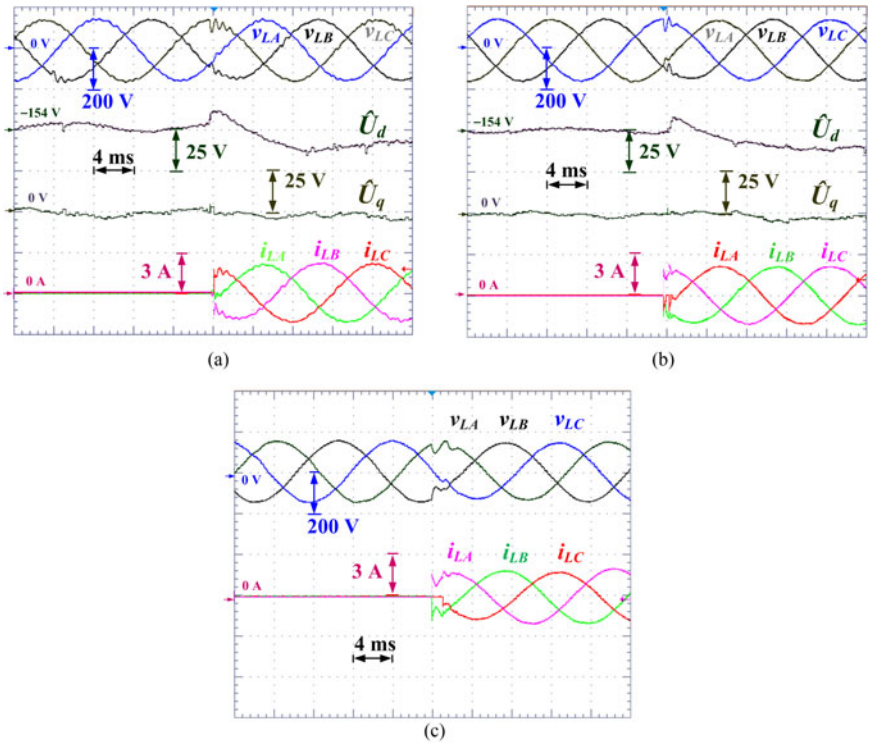

Fig. 9. Comparative experimental results in *Case 1* (i.e., load step-change from zero to full load). (a) Conventional FCS-MPC scheme. (b) Proposed MPC scheme. (c) Conventional nested-loop PI control scheme.

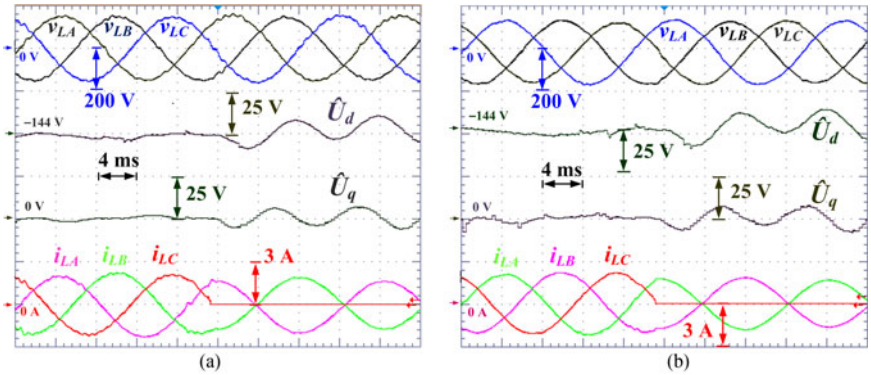

Fig. 10. Comparative experimental results in *Case 2* (i.e., unbalanced load with phase A suddenly opened). (a) Conventional FCS-MPC scheme. (b) Proposed MPC scheme.

is, the control design is built on the distorted parameters (i.e., $L = 1.5 \times 10 = 15$ mH, $C = 0.5 \times 6.6 = 3.3\,\mu$F).

Figs. 9–11 present the comparative experimental results of the conventional FCS-MPC scheme and the proposed MPC scheme under *Cases 1* to *3*, respectively. In each figure, the subfigures (a) and (b) show the experimental results of the conventional FCS-MPC scheme and the proposed MPC scheme, respectively. Each subfigure shows the three-phase load voltages ($\boldsymbol{V}_L = [v_{LA}, v_{LB}, v_{LC}]^T$), estimated disturbance vector in d–q components ($\hat{\boldsymbol{U}} = [\hat{U}_d, \hat{U}_q]^T$), and three-phase load currents ($\boldsymbol{I}_L = [i_{LA}, i_{LB}, i_{LC}]^T$). It is noted that only three kinds of waveforms are intentionally chosen in each subfigure because they can efficiently present the transient- and steady-state performances of each control scheme. That is, $\boldsymbol{V}_L$ and $\boldsymbol{I}_L$ illustrate the sinusoidal-shape waveforms that identify the sudden-change instants, qualitatively. Meanwhile, $\hat{\boldsymbol{U}}$ effectively shows the disturbances that significantly affect the control performances.

1) Transient- and Steady-State Performances Under Load Step Change with $+50\%L_f$ and $-50\%C_f$: Fig. 9(a) and (b) show the comparative performances between the conventional FCS-MPC scheme and the proposed MPC scheme under load step changes with $+50\%L_f$ and $-50\%C_f$, respectively.

In Fig. 9(a), the conventional FCS method shows the fast response properties with the recovering time within about 1 ms after the sudden disturbance. However, there are high ripples in the waveforms that cause longer settling time during the transient, higher THD (2.1%) at steady state, and especially larger SSE (1.4%) in the steady state considered as a typical drawback of the FCS-MPC scheme. On the other hand, the proposed

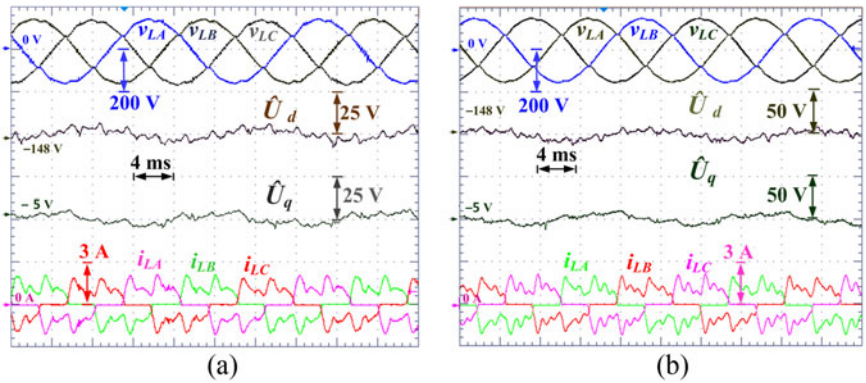

Fig. 11. Comparative experimental results in *Case 3* (i.e., nonlinear load with the crest factor = 2.90). (a) Conventional FCS-MPC scheme. (b) Proposed MPC scheme.

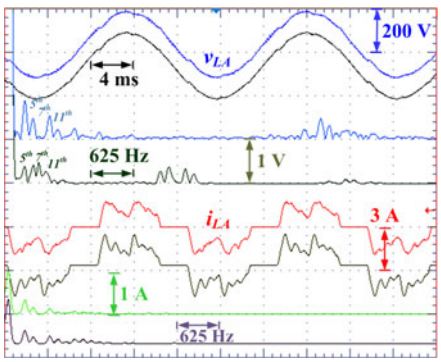

Fig. 12. Spectrum analysis of the load phase voltage and current for the conventional FCS-MPC scheme (upper positions) and the proposed MPC scheme (lower positions) in *Case 3* (i.e., nonlinear load with the crest factor = 2.90).

MPC scheme also exhibits the fast recovery time within about 1 ms as shown in Fig. 9(b). However, its output voltage quality is better with only 0.3% in SSE and about 0.8% in THD than the conventional FCS-MPC scheme. In Fig. 9(a) and (b), both schemes show small SSEs before and after sudden disturbance because the DOB successful catches up with the disturbance sources. Note that the steady-state error is the main drawback of the FCS-MPC [28] due to its heavy dependence on system parameters. Fig. 9(c) shows the comparative experimental results of the conventional nested-loop PI control scheme to validate the superiority of the proposed MPC scheme. In Fig. 9(c), the conventional nested-loop PI control method shows the following responses: recovering time (2.2 ms), THD (0.85%), and SSE (1.0%). In order to achieve a fair comparison, the PI gains of the conventional PI control scheme are retuned carefully using two gain settings as described in [18] by comparing its closed-loop response with the performance of the proposed MPC method shown in Fig. 6(c). Then the optimal performance of the conventional PI controller is achieved when any further tuning by increasing or decreasing these PI gains may degrade the control performance [18]. Finally, the comparative results in Fig. 9 validate the distinctive advantages of the proposed MPC scheme over the conventional methods due to the two-mode approach and the DOB. Note that if the PI gains are not tuned again under the parameter uncertainties, the control performances are not acceptable. Meanwhile, the proposed MPC method can work well without retuning effort due to the DOB.

2) Transient- and Steady-State Performances Under Unbalanced Load With $+50\%L_f$ and $-50\%C_f$: Fig. 10 shows the comparative results of the two control schemes with $+50\%L_f$ and $-50\%C_f$ when phase *A* is unexpectedly disconnected. In this figure, both the voltage controllers show very fast responses at the disturbance instant with nearly no change in the output waveforms (i.e., recovered within about 0.5 ms). However, the proposed MPC scheme show the better steady-state performances in Fig. 10(b) with much lower SSE (0.4%) and THD (0.65%) in comparison with the conventional FCS-MPC scheme (i.e., 2.2% and 1.8% in SSE and THD, respectively) shown in Fig. 10(a). In this case, the disturbance waveforms under unbalanced load show some ripples as a source of periodically varying disturbances. Nevertheless, these disturbances are compensated for to achieve the good performances on the output voltages as shown in Fig. 10.

3) Steady-State Performance Under Nonlinear Load With $+50\%L_f$ and $-50\%C_f$: Fig. 11 shows the comparative steady-state performance of the conventional FCS-MPC scheme and the proposed MPC scheme under a nonlinear load with $+50\%L_f$ and $-50\%C_f$. In this load condition, the output waveforms of both the control methods are distorted due to high-slope changes of the load currents caused by the three-phase diode rectifier. In this case, both the observers and the controllers have to deal with the fast changes of the load currents. Fig. 11(a) shows the waveforms of the conventional FCS-MPC scheme with 1.6% in SSE and 2.6% in THD, whereas Fig. 11(b) shows the performance of the proposed scheme with 0.4% in SSE and 1.2% in THD. In Fig. 11, the nonlinear load exhibits a fast varying disturbance and especially a high-slope disturbance (i.e., crest factor = 2.90) that causes the degradation on output control performances. It is noted that there are some distortions in the output waveforms causing high THDs at the instants when the disturbance sources abruptly change.

Fig. 12 depicts the spectrum analysis of the load phase voltage and current for the conventional FCS-MPC scheme (upper positions) and the proposed MPC scheme (lower positions) in *Case 3* (i.e., nonlinear load with the crest factor of 2.90). As shown in Fig. 12, the major harmonic contents of the fundamental frequency of 60 Hz are 5th, 7th, and 11th, and the proposed

TABLE I
QUANTITATIVE STEADY-STATE PERFORMANCE COMPARISON BETWEEN THE CONVENTIONAL SCHEME AND THE PROPOSED SCHEME

Investigated cases			Step change *Case 1*	Unbalanced *Case 2*	Nonlinear *Case 3*
Conventional FCS-MPC scheme					
Experiment	THD (%)		2.1	2.2	2.6
	SSE in RMS (%)	v_{LA}	1.4	1.4	1.6
		v_{LB}	1.3	1.8	1.6
		v_{LC}	1.3	1.8	1.5
Proposed MPC scheme					
Experiment	THD (%)		0.8	0.65	1.20
	SSE in RMS (%)	v_{LA}	0.3	0.2	0.4
		v_{LB}	0.2	0.4	0.4
		v_{LC}	0.3	0.4	0.3

MPC scheme shows smaller values of these harmonics than the conventional FCS-MPC scheme. In particular, the spectrum of the load voltage waveform of the conventional FCS-MPC scheme shows that higher harmonic contents are unpredictably distributed over the time and phase. These high harmonics make the filter design difficult and cause the EMI problems [2] because of its variable frequency. Furthermore, the unpredictably distributed harmonics and variable switching frequencies of the conventional FCS-MPC scheme result in uneven and variable switching loss-distribution over the switches and unwanted resonances due to the self-resonance frequency of the *LC* filter.

To quantitatively assess the experimental results (see Figs. 9–12) of the conventional FCS-MPC scheme and the proposed MPC scheme under three cases, Table I summarizes the steady-state performances with THDs- and RMS-based SSEs of the output voltages as widely used in [5], [10]–[12], [18]. As listed in Table I, the steady-state performances of the proposed MPC scheme show more advanced quality on the controlled outputs with low THDs and small SSEs compared with those of the conventional scheme. This can be achieved by the MOV with a continuous OV and the SVM as described in Section IV-C. It is worth noting that the proposed MPC scheme accomplishes the superior output quality with a fixed switching frequency of 5 kHz under parameter variations with $+50\%L_f$ and $-50\%C_f$.

VI. CONCLUSION

This paper proposes an efficient MPC method for three-phase inverter systems with output *LC* filters offering the following benefits: competitive output quality with a fixed switching frequency, robustness under system parameter uncertainties and variations, and fast dynamic responses with a simplified algorithm. The proposed approach focuses on directly solving a class of flexible optimization problems of the MPC with the analytical optimal solution (OV) for the unconstrained mode, using the MOV and limited control options to deal with the constraints while keeping the simplicity of the algorithm, and employing the SVM to fix the switching frequency. Furthermore, the KF-based optimal disturbance observer is designed to handle the parameter uncertainties and variations. This paper offers the analytical solution of the MPC optimization problem in the unconstrained mode and the near optimal solution in transient state. The comparative studies between the proposed MPC scheme, the deadbeat control law and the conventional FCS-MPC scheme are conducted in experiments to verify the effectiveness of the proposed MPC. In addition, the control strategy presented in this paper can be applied to various applications such as active power filter, dynamic voltage restorer, ac motor drives using switch-mode converters, etc.

REFERENCES

[1] J. M. Carrasco *et al.*, "Power-electronic systems for the grid integration of renewable energy sources: A Survey," *IEEE Trans. Ind. Electron.*, vol. 53, no. 4, pp. 1002–1016,Aug. 2006.

[2] S. Vazquez *et al.*, "Model predictive control: A review of its applications in power electronics," *IEEE Ind. Electron. Mag.*, vol. 8, no. 1, pp. 16–31, Mar. 2014.

[3] F. Blaabjerg, R. Teodorescu, M. Liserre, and A. V. Timbus, "Overview of control and grid synchronization for distributed power generation systems," *IEEE Trans. Ind. Electron.*, vol. 53, no. 5, pp. 1398–1409, Oct. 2006.

[4] J. Hu, J. Zhu, and D. G. Dorrell, "Model predictive control of inverters for both islanded and grid-connected operations in renewable power generations," *IET Renewable Power Gener.*, vol. 8, no. 3, pp. 240–248, Apr. 2014.

[5] E. K. Kim, F. Mwasilu, H. H. Choi, and J. W. Jung, "An observer-based optimal voltage control scheme for three-phase UPS systems," *IEEE Trans. Ind. Electron.*, vol. 62, no. 4, pp. 2073–2081, Apr. 2015.

[6] P. C. Loh, M. J. Newman, D. N. Zmood, and D. G. Holmes, "A comparative analysis of multiloop voltage regulation strategies for single and three-phase UPS systems," *IEEE Trans. Power Electron.*, vol. 18, no. 5, pp. 1176–1185, Sep. 2003.

[7] M. Shahparasti, M. Mohamadian, A. Yazdian, A. A. Ahmad, and M. Amini, "Derivation of a stationary-frame single-loop controller for three-phase standalone inverter supplying nonlinear loads," *IEEE Trans. Power Electron.*, vol. 29, no. 9, pp. 5063–5071, Sep. 2014.

[8] N. M. Abdel-Rahim and J. E. Quaicoe, "Analysis and design of a multiple feedback loop control strategy for single-phase voltage-source UPS inverters," *IEEE Trans. Power Electron.*, vol. 11, no. 4, pp. 532–541, Jul. 1996.

[9] G. Escobar, A. A. Valdez, J. Leyva-Ramos, and P. Mattavelli, "Repetitive-based controller for a UPS inverter to compensate unbalance and harmonic distortion," *IEEE Trans. Ind. Electron.*, vol. 54, no. 1, pp. 504–510, Feb. 2007.

[10] W. Lu, K. Zhou, D. Wang, and M. Cheng, "A general parallel structure repetitive control scheme for multiphase DC–AC PWM converters," *IEEE Trans. Power Electron.*, vol. 28, no. 8, pp. 3980–3987, Aug. 2013.

[11] H. K. Kang, C. H. Yoo, I. Y. Chung, D. J. Won, and S. I. Moon, "Intelligent coordination method of multiple distributed resources for harmonic current compensation in a microgrid," *J. Electr. Eng. Technol.*, vol. 7, no. 6, pp. 834–844, Nov. 2012.

[12] S. Jiang, D. Cao, Y. Li, J. Liu, and F. Z. Peng, "Low-THD, fast-transient, and cost-effective synchronous-frame repetitive controller for three-phase UPS inverters," *IEEE Trans. Power Electron.*, vol. 27, no. 6, pp. 2994–3005, Jun. 2012.

[13] O. Kukrer, H. Komurcugil, and A. Doganalp, "A three-level hysteresis function approach to the sliding mode control of single-phase UPS inverters," *IEEE Trans. Ind. Electron.*, vol. 56, no. 9, pp. 3477–3486, Sep. 2009.

[14] T. D. Do, V. Q. Leu, Y. S. Choi, H. H. Choi, and J. W. Jung., "An adaptive voltage control strategy of three-phase inverter for stand-alone distributed generation systems," *IEEE Trans. Ind. Electron.*, vol. 60, no. 12, pp. 5660–5672, Dec. 2013.

[15] D. Q. Dang, Y. S. Choi, H. H. Choi, and J. W. Jung, "Experimental validation of a fuzzy adaptive voltage controller for three-phase PWM inverter of a standalone DG unit," *IEEE Trans. Ind. Informat.*, vol. 11, no. 3, pp. 632–641, Jun. 2015.

[16] T. Kawabata, T. Miyashita, and Y. Yamamoto, "Dead beat control of three phase PWM inverter," *IEEE Trans. Power Electron.*, vol. 5, no. 1, pp. 21–28, Jan. 1990.

[17] P. Mattavelli, "An improved deadbeat control for UPS using disturbance observers," *IEEE Trans. Ind. Electron.*, vol. 52, no. 1, pp. 206–212, Feb. 2005.

[18] J. S. Lim, C. Park, J. Han, and Y. I. Lee, "Robust tracking control of a three-phase DC–AC inverter for UPS applications," *IEEE Trans. Ind. Electron.*, vol. 61, no. 8, pp. 4142–4151, Aug. 2014.

[19] P. Cortés, G. Ortiz, J. I. Yuz, J. Rodrisguez, S. Vazquez, and L. G. Franquelo, "Model predictive control of an inverter with output LC filter for UPS applications," *IEEE Trans. Ind. Electron.*, vol. 56, no. 6, pp. 1875–1883, Jun. 2009.
[20] S. K. Kim, C. R. Park, T. W. Yoon, and Y. I. Lee, "Disturbance-observer-based model predictive control for output voltage regulation of three-phase inverter for uninterruptible-power-supply applications," *Eur. J. Control*, vol. 23, pp. 71–83, May 2015.
[21] T. Geyer and D. Quevedo, "Multistep finite control set model predictive control for power electronics," *IEEE Trans. Power Electron.*, vol. 29, no. 12, pp. 6836–6846, Dec. 2014.
[22] R. Sultana and S. K. Sahoo, "Finite control set model predictive current control for a cascaded multilevel inverter," *J. Electr. Eng. Technol.*, vol. 11, no. 6, pp. 1674–1683, Nov. 2016.
[23] M. P. Akter, "Model predictive control of bidirectional AC–DC converter for energy storage system," *J. Electr. Eng. Technol.*, vol. 10, no. 1, pp. 165–175, Jan. 2015.
[24] Z. Song, Y. Tian, W. Chen, Z. Zou, and Z. Chen, "Predictive duty cycle control of three-phase active-front-end rectifiers," *IEEE Trans. Power Electron.*, vol. 31, no. 1, pp. 698–710, Jan. 2016.
[25] R. Aguilera and D. Quevedo, "Predictive control of power converters: Designs With guaranteed performance," *IEEE Trans. Ind. Informat.*, vol. 11, no. 1, pp. 53–63, Feb. 2015.
[26] J. H. Lee, "Model predictive control: Review of the three decades of development," *Int. J. Control Autom. Syst.*, vol. 9, no. 3, pp. 415–424, Jun. 2011.
[27] H. A. Young, M. A. Perez, J. Rodriguez, and H. Abu-Rub, "Assessing finite-control-set model predictive control: A comparison with a linear current controller in two-level voltage source inverters," *IEEE Ind. Electron. Mag.*, vol. 8, no. 1, pp. 44–52, Mar. 2014.
[28] J. Rodriguez *et al.*, "State of the art of finite control set model predictive control in power electronics," *IEEE Trans. Ind. Informat.*, vol. 9, no. 2, pp. 1003–1016, May 2013.
[29] S. Mariethoz and M. Morari, "Explicit model-predictive control of a PWM inverter with an LCL filter," *IEEE Trans. Ind. Electron.*, vol. 56, no. 2, pp. 389–399, Feb. 2009.
[30] R. P. Aguilera, P. Lezana, and D. E. Quevedo, "Switched model predictive control for improved transient and steady-state performance," *IEEE Trans. Ind. Informat.*, vol. 11, no. 4, pp. 968–977, Aug. 2015.
[31] R. Baidya *et al.*, "Fast multistep finite control set model predictive control for transient operation of power converters," in *Proc. 42nd Annu. Conf. IEEE Ind. Electron. Soc.*, Florence, Italy, Oct. 2016, pp. 5039–5045.
[32] M. Nauman and A. Hasan, "Efficient implicit model-predictive control of a three-phase inverter with an output LC filter," *IEEE Trans. Power Electron.*, vol. 31, no. 9, pp. 6075–6078, Sept. 2016.
[33] M. Tomlinson, H. T. Mouton, R. Kennel, and P. Stolze, "A fixed switching frequency scheme for finite-control-set model predictive control—concept and algorithm," *IEEE Trans. Ind. Electron.*, vol. 63, no. 12, pp. 7662–7670, Dec. 2016.
[34] K. Ogata, *Discrete-Time Control Systems*, 2nd ed. Englewood Cliffs, NJ, USA: Prentice-Hall, 1994.
[35] D. E. Quevedo, R. P. Aguilera, and T. Geyer, *Predictive Control in Power Electronics and Drives: Basic Concepts, Theory, and Methods, Advanced and Intelligent Control in Power Electronics and Drives*, vol. 531. New York, NY, USA: Springer-Verlag, 2014, no. 5, pp. 181–226.

Hoach The Nguyen received the B.S. degree in electrical engineering from Hanoi University of Science and Technology, Hanoi, Vietnam, in 2007, and the M.S. degree in electrical engineering from Dayeh University, Changhua, Taiwan, in 2010. He is currently working toward the Ph.D. degree in the Division of Electronics and Electrical Engineering, Dongguk University, Seoul, South Korea.

From 2011 to 2014, he was with Hanoi Architecture University, Hanoi, Vietnam, as a Lecturer. His current research interests include electric power system, control of power converters, and DSP-based electric machine drives.

Eun-Kyung Kim received the B.S. degree in electrical engineering from Dongguk University, Seoul, South Korea, in 2009. She is currently working toward the Ph.D. degree in the Division of Electronics and Electrical Engineering, Dongguk University.

From 2009 to 2012, she was in the Electrical Vehicle Research Laboratory, VCTech Company, Ltd., Gyeonggi, South Korea. Her current research interests include digital signal processor-based electric machine drives, electric vehicles, smart grid enabling technologies, and control of distributed generation systems using renewable energy sources.

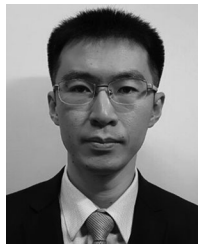

Ik-Pyo Kim received the B.S. degree in electrical engineering from Ulsan University, Ulsan, South Korea, in 2001, and the M.S. degree in new and renewable energy engineering from Dongguk University, Seoul, South Korea, in 2012. He is currently working toward the Ph.D. degree in the Department of New & Renewable Energy Engineering, Dongguk University.

From 2001 to 2004, he was a Research Engineer with the Mobile RF team, Samsung Electro-Mechanics Co., Ltd., Suwon, South Korea. Since 2004, he has been a Senior Manager of New & Renewable Energy Promotion Division, Korea Energy Agency, Yongin, South Korea. His current research interests include photovoltaic power system, energy storage system, renewable energy technology standards and certification, and renewable energy policy and program evaluation.

Han Ho Choi (M'03) received the B.S. degree in control and instrumentation engineering from Seoul National University, Seoul, South Korea, in 1988, and the M.S. and Ph.D. degrees in electrical engineering from the Korea Advanced Institute of Science and Technology, Daejeon, South Korea, in 1990 and 1994, respectively.

He is currently in the Division of Electronics and Electrical Engineering, Dongguk University, Seoul, South Korea. His current research interests include control theory and its application to real-world problems.

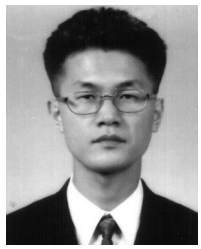

Jin-Woo Jung (M'06) received the B.S. and M.S. degrees in electrical engineering from Hanyang University, Seoul, South Korea, in 1991 and 1997, respectively, and the Ph.D. degree in electrical and computer engineering from the Ohio State University, Columbus, OH, USA, in 2005.

From 1997 to 2000, he was in the Home Appliance Research Laboratory, LG Electronics Co., Ltd., Seoul, South Korea. From 2005 to 2008, he was a Senior Engineer in the R&D Center and with the PDP Development Team, Samsung SDI Co., Ltd., South Korea. Since 2008, he has been a Professor in the Division of Electronics and Electrical Engineering, Dongguk University, Seoul, South Korea. His current research interests include DSP-based electric machine drives, distributed generation systems using renewable energy sources, and power conversion systems and drives for electric vehicles.